Benchmarking Inorganic Deposition Routes for Hybrid Two-Step Processed Perovskite Solar Cells: A Materials Perspective

Julian Petry[1,2,*], Ronja Pappenberger[1,2,*], Alexander Welle[3,4], Tonghan Zhao[1], Alexander Diercks[2], Raphael Pesch[1,2], Paul Fassl[1,2], and Ulrich W. Paetzold[1,2]

[1]Institute of Microstructure Technology (IMT), Karlsruhe Institute of Technology (KIT), Hermann-von-Helmholtz-Platz 1, 76344 Eggenstein-Leopoldshafen, Germany
[2]Light Technology Institute (LTI), Karlsruhe Institute of Technology (KIT), Engesserstrasse 13, 76131 Karlsruhe, Germany
[3]Institute of Functional Interfaces (IFG), Karlsruhe Institute of Technology (KIT), Hermann-von-Helmholtz-Platz 1, 76344 Eggenstein-Leopoldshafen, Germany
[4]Karlsruhe Nano Micro Facility (KNMFi), Karlsruhe Institute of Technology (KIT), Hermann-von-Helmholtz-Platz 1, 76344 Eggenstein-Leopoldshafen, Germany

E-Mail:
julian.petry@kit.edu; ronja.pappenberger@kit.edu; paul.fassl@kit.edu; ulrich.paetzold@kit.edu

*These authors contributed equally to this work

Keywords: perovskite solar cell, hybrid route, vacuum-based deposition, co-deposition, sequential deposition, materials characterization, morphology, microstructure, crystallinity

Abstract

As the perovskite solar cell (PSC) industry moves toward large-scale manufacturing, production processes must enable high-throughput fabrication and simple process integration. The hybrid two-step deposition route has emerged as a promising method for achieving conformal coatings on micron-scale textures, a critical feature for perovskite/silicon tandem photovoltaics. In this work, we present a fully sequential route, wherein the inorganic materials CsCl and PbI_2 are deposited separately, allowing for facile industrial implementation as compared to the commonly co-deposited inorganic scaffold. Microstructural analysis reveals a change in preferred crystal orientation of the PbI_2 platelets with co-deposition resulting in horizontal growth, whereas sequential deposition promotes vertical growth with a secondary tilted orientation. Further analysis of the elemental distribution in the final perovskite film reveals significant ion diffusivity for Cs, formamidinium and I, which are distributed homogeneously throughout the final perovskite absorber. Contrary, Pb and Cl ions exhibit a lower ion diffusivity, with spatial distributions largely retained from the initial inorganic scaffold. For PSCs with 1.69 eV bandgap, PCEs of 19.3% and 18.7% are achieved for co-deposition and sequential deposition, respectively, underscoring the potential of fully sequential hybrid deposition as a viable route toward industrial PSC production.

1 Introduction

Perovskite solar cells (PSCs) have demonstrated an unprecedented progress in achieved power conversion efficiency (PCE) over the past decade. Since their first report in 2009 with a PCE of 3.8%, single-junction PSCs approach an efficiency of 27% today, positioning them as strong future competitor to established silicon (Si) photovoltaic technologies.[1, 2] In particular, inverted PSCs (*p-i-n* architecture) have attracted significant interest due to their compatibility with p-type Si bottom cells in monolithic tandem configuration. Perovskite/silicon tandem solar cells (TSCs) have already surpassed the theoretical efficiency limit of single-junction Si solar cells,[3] achieving record efficiencies exceeding 34%,[2] and are considered as promising candidates for next-generation, high-efficiency photovoltaic modules[4–9] – given that remaining stability challenges are resolved.[10]

Commercial Si bottom cells typically feature random pyramidal textures (2-5 µm in height), exhibiting enhanced light-harvesting properties compared to planar or polished surfaces.[11–16] However, depositing uniform, high-quality perovskite layers on such textured surfaces remains challenging – a critical requirement for industrial-scale monolithic tandem integration.[4] Conventional solution-based methods struggle to provide conformal coating on micron-scale textures, often resulting in poor surface coverage and reduced device performance.[17, 18] Alternatively, vacuum-based deposition methods offer conformal coating on textured substrates as well as the possibility for large-scale deposition.[19–22] A major drawback is the notoriously difficult control of the volatile organic components, suffering from poor process repeatability.[23–28] Additionally, vacuum-based deposition of organic precursor materials can pose a critical bottleneck for the achievable deposition rates, limiting fabrication throughput.[29] To address these challenges, hybrid two-step deposition routes have emerged, combining conformal vacuum-based deposition of the inorganic precursors with a subsequent solution-based deposition of the organic cations. This method allows for enhanced compositional flexibility, facile introduction of additives and the exclusive usage of green solvents.[17, 30–34] Several studies have extended the knowledge on perovskite film formation using the hybrid two-step deposition route in both single-junction[33, 35–39] and tandem configuration, for which PCEs above 31% have been demonstrated on micron-scale textured Si bottom cells.[40, 41] A first study on a large area perovskite/silicon TSC reached a promising PCE of close to 28% using blade-coating as a scalable solution-based deposition method.[42]

While scalable coating techniques are essential, a major challenge for the industrial adaptation of PSCs is the need for high-throughput fabrication. In a previous work, we demonstrated that in case of vacuum deposition, the sequential deposition of all precursor materials is desired for high-throughput solar cell fabrication, allowing for the maximum deposition rates of the individual sources thus offering the highest process effectiveness.[29] In contrast, co-deposition requires precise control over the relative sublimation rates of multiple materials, complicating process metrology and limiting throughput.[29] To the best of our knowledge, current studies using the hybrid two-step route rely exclusively on co-deposition of the inorganic scaffold, whereby sequential deposition has not yet been reported, which may hinder direct transfer to industrial production.

In this work, we present a fully sequential vacuum-based deposition route of the inorganic scaffold for the hybrid two-step deposition route for wide-bandgap single-junction PSCs. We benchmark the sequential deposition route against the conventional co-deposition route and demonstrate comparable PCEs of 19.3% and 18.7% for co- and sequential deposition, respectively. Despite the comparable device performance, the sequential deposition route has prospects in simplifying process integration and scalability, making it a more favorable option for the industrial fabrication of PSCs. Detailed structural analysis reveals distinct differences in the morphology and crystal orientation of the inorganic scaffolds. Further, a strong influence of the elemental distribution depending on the deposition route is indicated, highlighting a pronounced layer structure in the sequentially deposited inorganic scaffold. In summary, our findings underscore the material-level impact of the deposition

route already at a fundamental level.

2 Results and Discussion

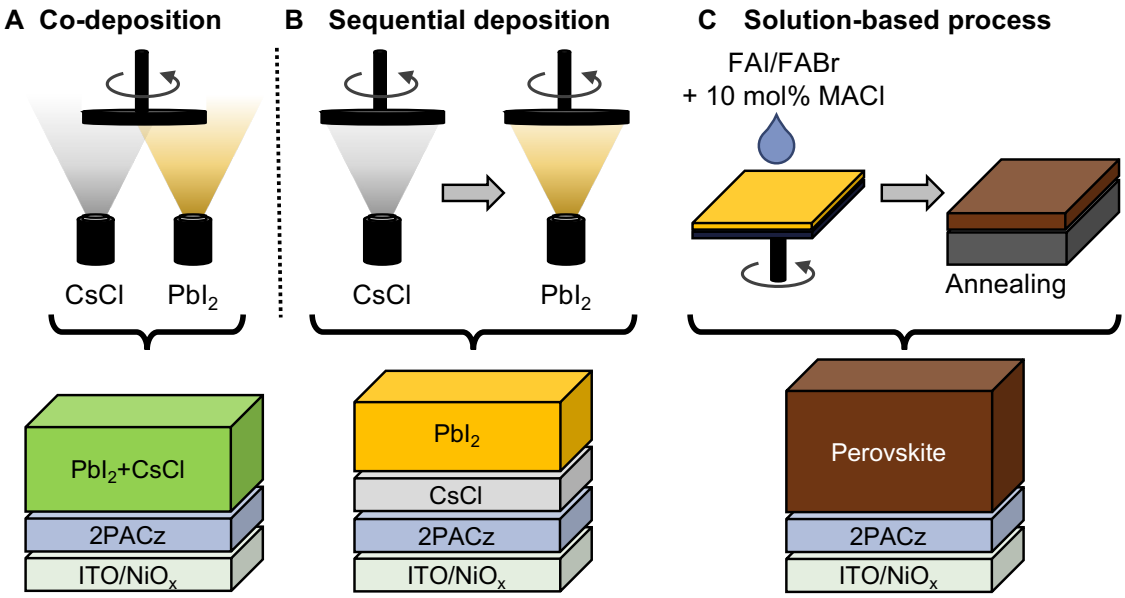

Figure 1: Schematic of the two hybrid two-step deposition routes studied in this work: **A** co-deposition (Co) and **B** sequential deposition (Seq) routes of the inorganic precursors CsCl and PbI_2, with the corresponding layer sequence depicted below each process. **C** Schematic illustration of the final perovskite thin film obtained after deposition of the organic cation solution and subsequent thermal annealing under ambient conditions.

The hybrid two-step deposition route encompasses the vacuum-based deposition of the inorganic precursors, followed by a solution-based deposition of the organic precursors. The schematics for both co-deposition (**Figure** 1 A, labeled as Co) and sequential deposition (Figure 1 B, labeled as Seq) of the inorganic precursor materials PbI_2 and CsCl are illustrated in Figure 1. The incorporation of CsCl into the inorganic scaffold was shown to promote crystallization and enhance the overall quality of the resulting perovskite film.[43] In co-deposition, both inorganic precursor materials are sublimated simultaneously. For sequential deposition, CsCl is deposited first, followed by a subsequent deposition of PbI_2. Conversion to the final perovskite absorber is realized by depositing the organic cation solution *via* spin-coating, based on an established recipe introduced by Li *et al.*[31] and Er-raji *et al.*[33], followed by thermal annealing under ambient conditions (Figure 1 C). We adapt a NiO_x/2PACz bilayer as *p*-selective contact, which was found to improve hole extraction and perovskite crystal quality, compared to the reference with only 2PACz.[44] The resulting half-stack devices comprise the layer sequence glass/ITO/NiO_x/2PACz/perovskite. In this study, the perovskite absorber has a nominal composition of $Cs_{0.18}FA_{0.82}Pb(I_{0.76}Br_{0.18}Cl_{0.06})_3$ with a target bandgap of 1.69 eV (Figure S1). Further details on the fabrication method of the PSCs are described in the Experimental Section.

2.1 Photovoltaic Performance of Perovskite Solar Cells

Despite the very different process sequence, comparable device performances are observed for PSCs fabricated with both co- (Co) and sequential (Seq) deposition of the inorganic scaffold.

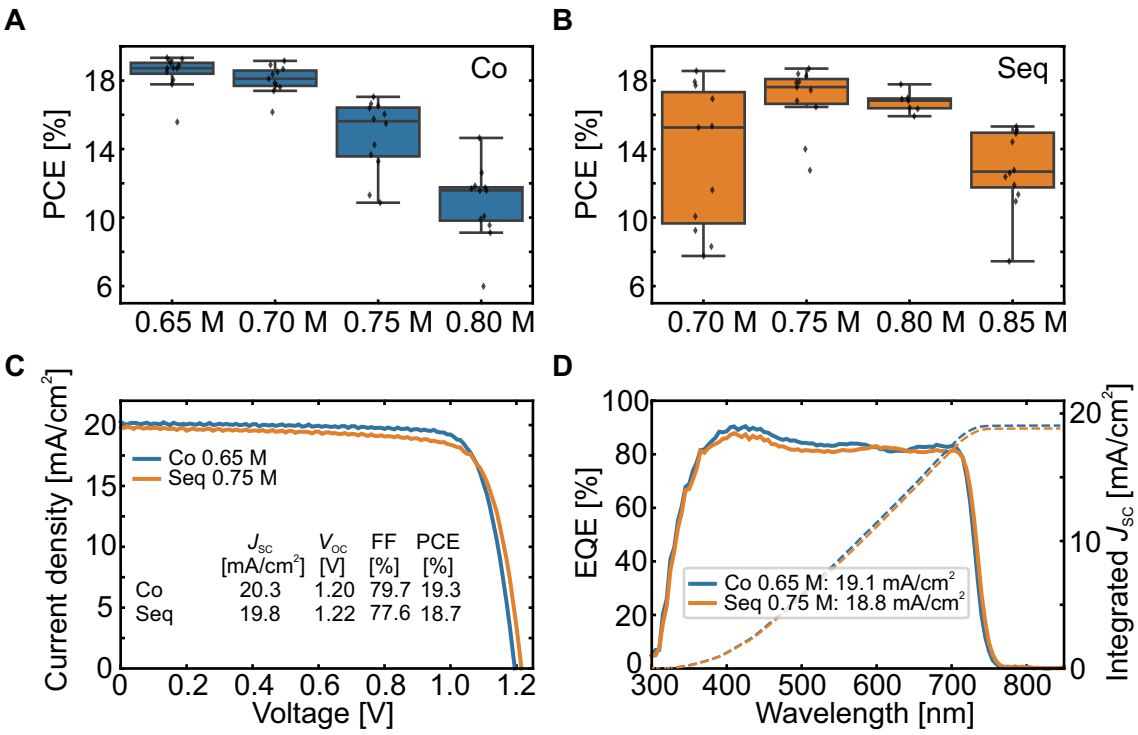

Figure 2: Statistical distribution of the power conversion efficiency (PCE) for perovskite solar cells (PSCs) with **A** co- (Co) and **B** sequential (Seq) deposition of the inorganic scaffold for different molarities of the organic cation solution. **C** Current density versus voltage (*J-V*) characteristics and **D** external quantum efficiency (EQE) spectra, along with the corresponding integrated short-circuit current density (J_{SC}), for the champion devices fabricated with co- or sequential deposited inorganic scaffold (optimal molarity of the organic cation solution).

In order to allow a fair comparison of optimal thin film conversion for both deposition routes, the conversion of the inorganic scaffold to the perovskite absorber is optimized by varying the molarity of the organic cation solutions in a range of 0.65 M to 0.85 M of formamidinium iodide (FAI)/formamidinium bromide (FABr) with 10 mol% of methylammonium chloride (MACl) as an additive. The statistical results are shown in **Figure** 2 A/B and in Figure S2 and Figure S3. At the optimal organic cation molarity, champion PCEs of 19.3% in the backward scan (19.0% in the forward scan) and 18.7% (17.9%) are achieved for co-deposition (0.65 M) and sequential deposition (0.75 M), respectively (Figure 2 C, Figure S4 and Table S1). These results are comparable to the highest reported in literature for a bandgap of 1.69 eV.[32, 39, 40, 45] *Welch's t-test* confirms that V_{OC} and J_{SC} do not differ significantly between the two deposition routes, indicating a comparable efficiency in photogeneration and charge separation (Table S2).
Since both the device architecture and absorption spectra (Figure S5) are consistent across all devices, similar charge carrier extraction can be assumed. This is further corroborated by external quantum efficiency (EQE) measurements, showing a similar spectral response with integrated short-circuit current densities of 19.1 and 18.8 mA/cm^2 for co-deposition and sequential deposition, respectively.

2.2 Layer Morphology and Microstructure

The morphology and microstructure of the inorganic scaffold exhibit pronounced and systematic differences depending on the deposition route used. These differences are readily apparent upon visual inspection: co-deposition of the inorganic scaffold yields a smooth surface appearance, while sequential deposition produces a distinctly rougher surface (Figure S6). This change in morphology motivates a more detailed investigation using scanning

electron microscopy (SEM) and atomic force microscopy (AFM), as shown in **Figure** 3. SEM analysis reveals pronounced morphological differences in the inorganic scaffolds (Figure 3 A/B), correlating the macroscopic surface appearance with microstructural characteristics. The co-deposited inorganic scaffold exhibits a dense, uniform morphology with a smooth surface and a thickness of approximately 330 nm, consistent with quartz crystal microbalance (QCM) measurements and surface profilometry (Table S3 and Figure S7). Individual PbI_2 platelets are not discernible in this case. In contrast, the sequentially deposited inorganic scaffold displays a markedly irregular surface structure, making precise thickness determination challenging. A higher average layer thickness of 409 ± 4 nm is measured with surface profilometry. Sequential deposition of both precursor materials leads to a highly textured microstructure with vertical alignment of PbI_2 platelets, clearly visible in both top-view and cross-section SEM images. Two predominant orientations – either vertical or tilted with respect to the substrate – are apparent.

AFM measurements further support these findings, highlighting a significant difference in surface roughness between the two deposition routes: the co-deposited inorganic scaffold exhibits a ten times lower root-mean-square (RMS) surface roughness of 6.1 ± 0.1 nm compared to 77.1 ± 0.4 nm for the sequentially deposited inorganic scaffold. The surface roughness of the inorganic scaffold is an indication of the porosity of the layer, positively impacting the absorption of the organic cation solution into the inorganic scaffold.[46] To assess this, surface structure analysis of a picoliter drop dispensed on the inorganic scaffold is conducted *via* confocal scanning microscopy (Figure S8). On the co-deposited inorganic scaffold, residual crystalline organic salts accumulate at the center of the dried droplet, indicating limited droplet absorption. In contrast, the sequentially deposited inorganic scaffold shows improved droplet absorption, with less visible organic salt residue remaining.

Despite the very different morphology of the inorganic scaffold, the final perovskite thin films – fabricated by spin-coating the optimal molarity of the organic cation solution – exhibit no significant difference in thin film morphological between both deposition routes (Figure 3 C/D). Top-view and cross-section SEM images reveal a comparable microstructure, supported by AFM analysis indicating similar RMS surface roughness values of 29.6 ± 0.7 nm and 26.8 ± 0.3 nm for co-deposition and sequential deposition, respectively. Interestingly, surface profilometry reveals a substantially higher perovskite layer thickness for the sequential deposition route, increasing from 524 ± 4 nm for the co-deposition route to 682 ± 5 nm (Table S3 and Figure S7). The expansion coefficients ($\text{thickness}_{\text{perovskite}}/\text{thickness}_{\text{inorganic}}$) for co-deposition and sequential deposition are 1.62 and 1.67, respectively, indicating a slightly increased uptake of organic cations in the case of sequentially deposited inorganic scaffolds.

In summary, while the deposition route has a substantial impact on the morphology and microstructure of the inorganic scaffold, the morphology of the resulting perovskite absorber layer remains comparable.

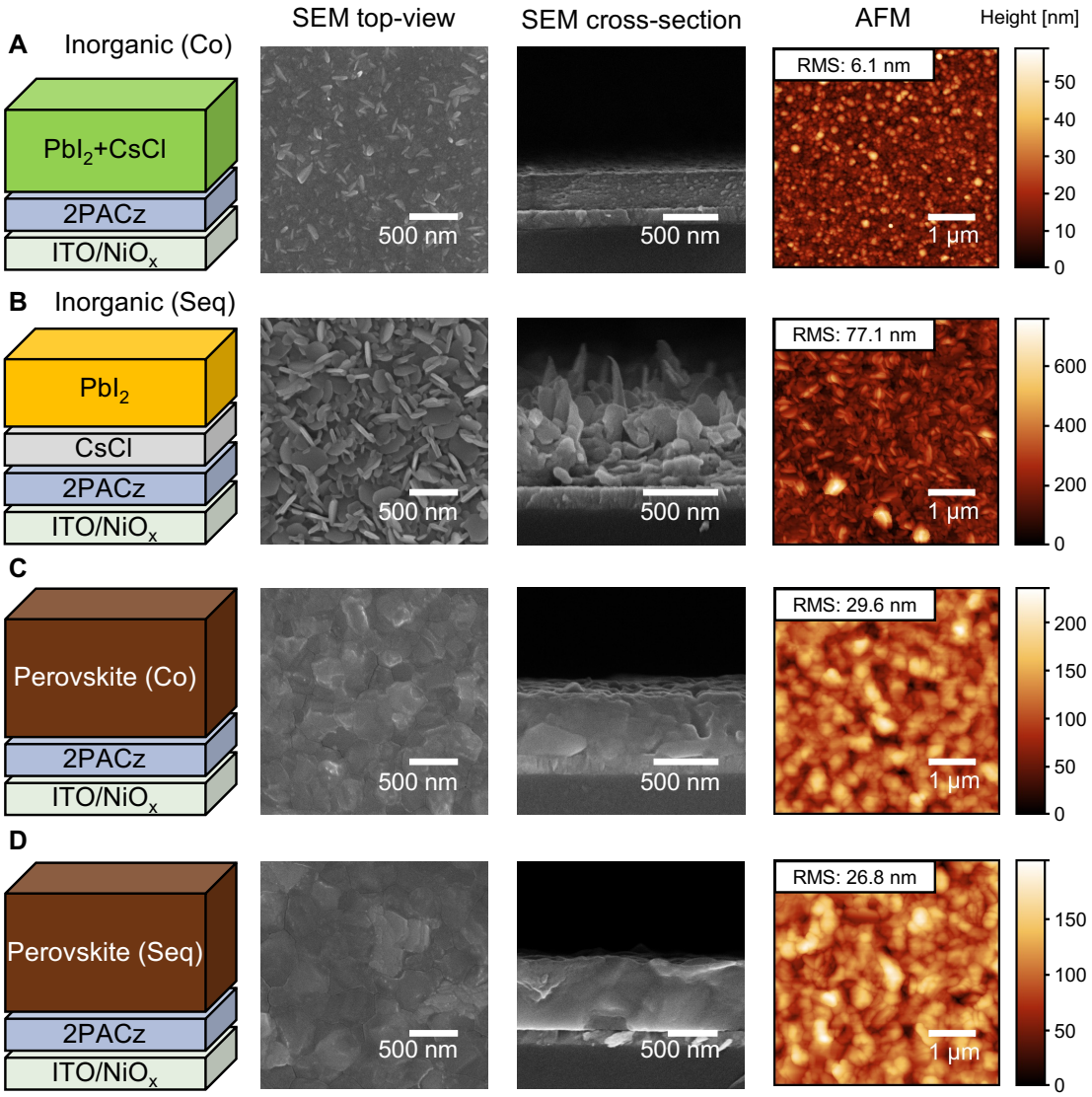

Figure 3: Scanning electron microcopy (SEM) images (top-view and cross-section) and atomic force microscopy (AFM) images of the inorganic scaffold deposited by **A** co- (Co) and **B** sequential (Seq) deposition, as well as of the corresponding perovskite films with **C** co- (Co) and **D** sequential (Seq) deposition of the inorganic scaffold. For the perovskite films, the optimal molarity of the organic cation solution is used.

2.3 Crystal Orientation

The crystal growth orientation of the inorganic scaffold, and consequently the growth behavior of the resulting perovskite absorber is influenced by the deposition route. To further analyze the effect of the deposition route on the microstructural properties of the inorganic scaffold as well as the final perovskite film, grazing-incidence wide-angle X-ray scattering (GIWAXS) measurements are performed (**Figure** 4). GIWAXS provides insight into the preferred growth direction and overall crystallinity of thin films.[47]

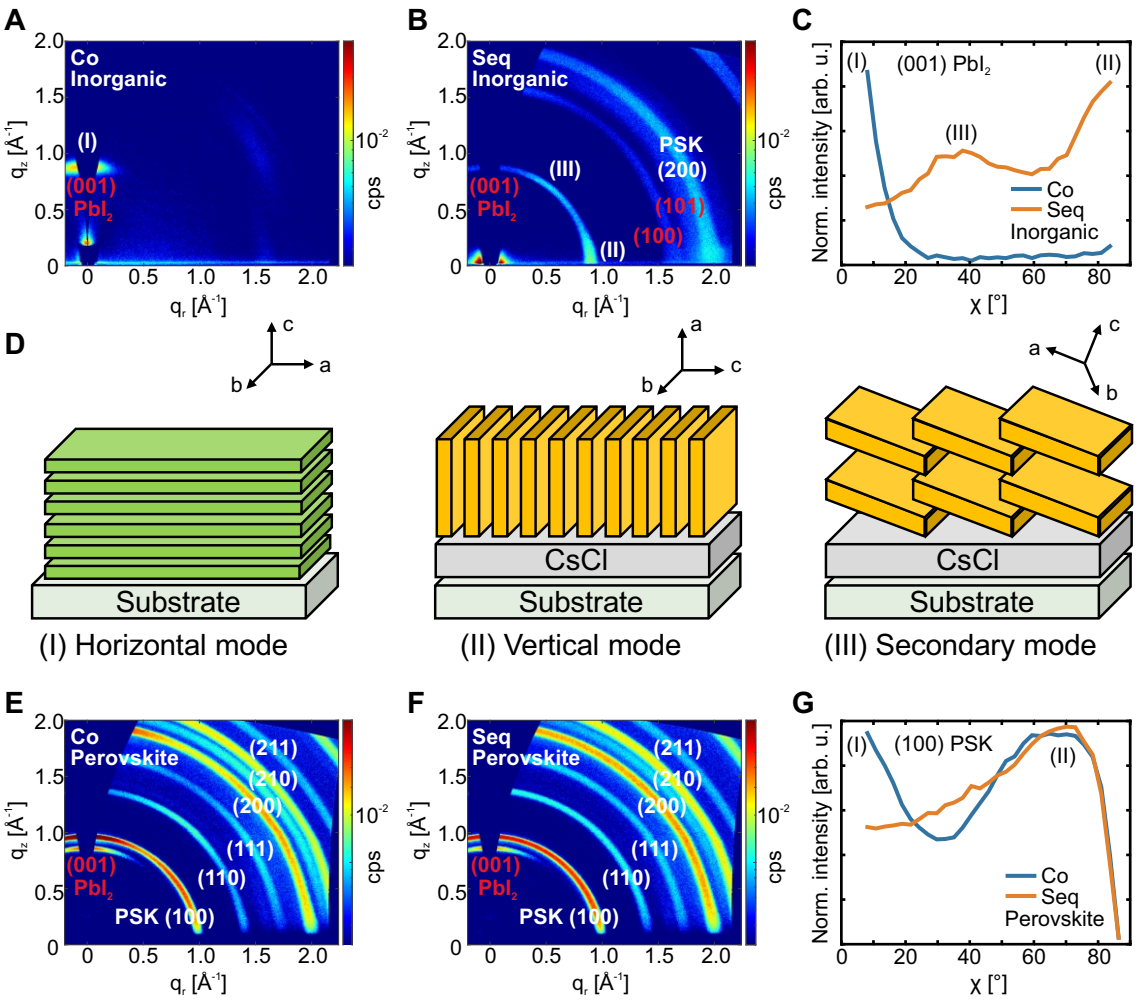

Figure 4: Grazing-incidence wide-angle X-ray scattering (GIWAXS) patterns of the inorganic scaffold deposited by **A** co- (Co) and **B** sequential (Seq) deposition, and of the final perovskite films prepared using **E** co- (Co) and **F** sequential (Seq) deposition of the inorganic scaffold. **D** Schematic illustration depicting the orientation of the PbI_2 platelets in the inorganic scaffold for co-deposition **(I)** and sequential deposition **(II)**/**(III)**. Distribution of crystallite orientation of the (001) PbI_2 plane in the inorganic scaffolds **C** and (100) perovskite plane in the final perovskite films **G**. For the perovskite films, the optimal molarity of the organic cation solution is used.

Considering the inorganic scaffold, a change in the preferred orientation of the (001) PbI_2 crystal plane is observed from selective growth in the out-of-plane orientation for co-deposition to preferred in-plane orientation for sequential deposition as shown in Figure 4 A/B. This change in orientation results in a horizontal layer growth of PbI_2 platelets for co-deposition and a tendency towards vertical layer growth for sequential deposition, aligning with the observations from SEM analysis (Figure 3). The corresponding distribution of crystallite orientation with integrated intensity over the azimuth angle χ of the (001) PbI_2 crystal plane with a scattering vector of q=0.9 $Å^{-1}$ is shown in Figure 4 C. The addition of CsCl in the co-deposition route enforces an exclusive horizontal alignment of the (a,b)-plane of PbI_2 relative to the substrate as illustrated in Figure 4 D, which is defined as the horizontal mode (I). A similar preferred orientation is found by Meng *et al.* when depositing pure PbI_2 *via* a spin-coating route.[48] In contrast, sequential deposition yields a preferred vertical growth, with the (a,b)-plane of PbI_2 vertical relative to the substrate (vertical mode (II), Figure 4 D), which appears to be the intrinsic growth mode for pure PbI_2 in vacuum-based deposition processes. We hypothesize, that the PbI_2 growth along the (a,b)-plane is thermodynamically preferred, as impinging PbI_2 molecules

are bound through ionic forces, whereas the growth along the c-axis is governed by weaker van der Waals forces. Additionally, a secondary preferred growth mode is observed for sequentially deposited inorganic layers with the (a,b)-plane oriented around 40° relative to the substrate (secondary mode (III), Figure 4 D). This is consistent with findings by Diercks *et al.*, who compared the surface dependent growth of pure PbI_2 on different HTL systems observing a similar secondary orientation at 40° for PTAA, NiO_x and TaTm.[49] The exact growth mechanism resulting in the surface dependent appearance of the secondary preferred growth direction remains elusive, requiring further investigation, which is beyond the scope of this study.
For the sequentially deposited inorganic scaffold, the GIWAXS signal with scattering vector of q=2.0 $Å^{-1}$ aligns with the expected signal of the (200) perovskite phase and is likewise detected in the corresponding X-ray diffraction (XRD) measurements (Figure S9). This suggests that interfacial reactions between CsCl and PbI_2 may initiate partial perovskite formation.
The corresponding perovskite films are also analyzed by GIWAXS measurements, revealing a subtle difference in the preferred crystal orientation of the (100) perovskite phase (Figure 4 E/F/G). Both perovskite films exhibit a discrete Bragg spot around 70°, indicating that it is the intrinsic perovskite growth mode. Interestingly, a secondary small angle Bragg peak is observed exclusively for the co-deposition route (pole figure of the (100) perovskite plane in Figure 4 G). We hypothesize that this is due to a templating effect from the horizontally aligned PbI_2 platelets of the inorganic scaffold, which likely undergo topotactic reaction – preserving the crystallographic orientation from the precursor phase.[50, 51]
Complementary XRD measurements of the inorganic layers confirm that the crystal orientation is strongly influenced by the deposition route. Specifically, the (001) PbI_2 diffraction peak is more prominent in the co-deposited inorganic layer, while the (003) PbI_2 peak is more pronounced in the sequentially deposited inorganic layer (Figure S9). In the resulting perovskite films, similar diffraction peaks with comparable peak intensities and peak area ratios are observed for both deposition routes (Figure S10 and S11). However, the (110) and (111) perovskite peaks appear more pronounced relative to the (100) perovskite peak in perovskite films derived from sequential deposition. Notably, the peak ratio of the (100) perovskite peak to the (001) PbI_2 peak, as well as the full width at half maximum (FWHM) of the (100) perovskite peak, correlate with the molarity of the organic cation solution, highlighting the importance of optimizing the precursor ratio for best device performance (Figure S10 and S11).
In summary, the deposition route has a profound influence on the crystal growth orientation of the inorganic scaffold. These differences partially carry over to the perovskite thin film, suggesting that the initial alignment of the PbI_2 platelets plays a templating role during perovskite formation.

2.4 Elemental Distribution

The deposition route considerably influences the elemental distribution and inter diffusion behavior within the inorganic scaffold and the resulting perovskite absorber layer. To probe the qualitative elemental distribution as a function of depth, a series of time-of-flight secondary ion mass spectrometry (ToF-SIMS) depth profiles are conducted. Characteristic positively charged secondary ions of the relevant species for the inorganic scaffolds and the final perovskite film are displayed in **Figure** 5 A/B and Figure 5 C/D, respectively.

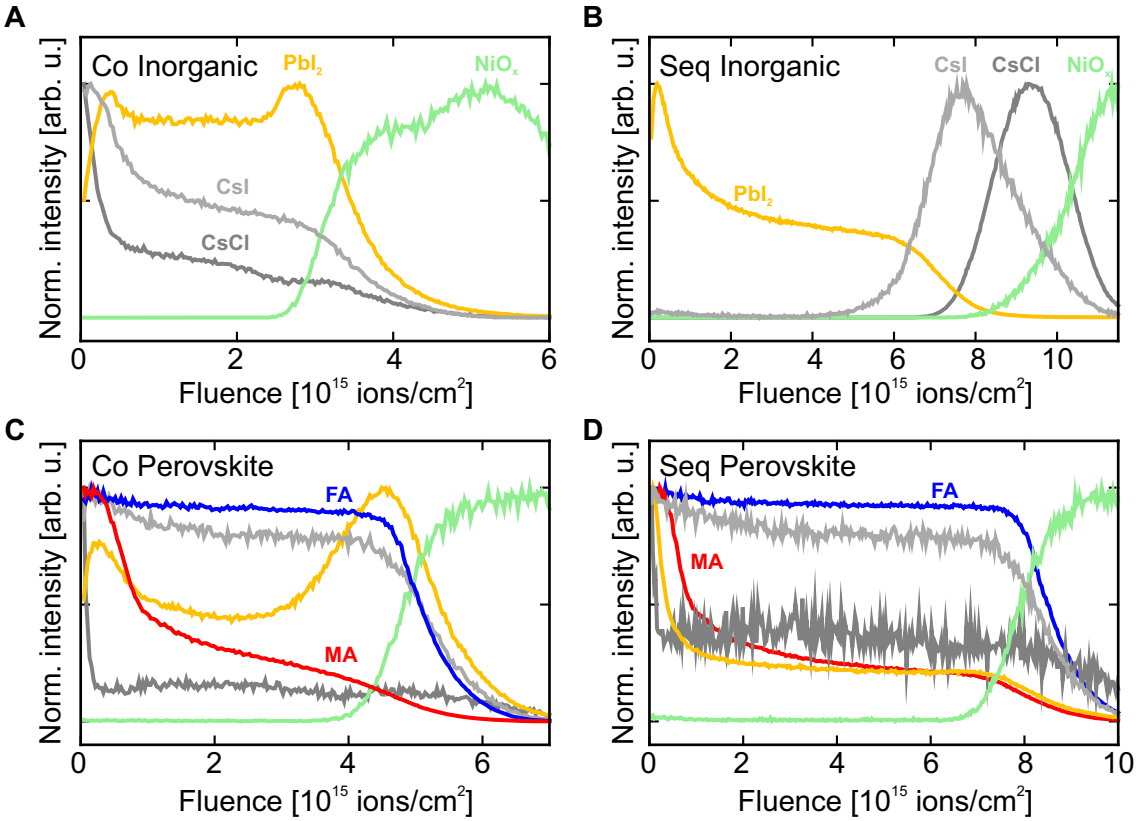

Figure 5: Normed time-of-flight secondary ion mass spectrometry (ToF-SIMS) measurements (positive polarity) of the inorganic scaffold deposited by **A** co- (Co) and **B** sequential (Seq) deposition, and of the final perovskite films prepared using **C** co- (Co) and **D** sequential (Seq) deposition of the inorganic scaffold. For the perovskite films, the optimal molarity of the organic cation solution is used. The following fragments are displayed: NiO_x: $\Sigma(^{58}Ni^+,^{60}Ni^+)$; PbI_2: $\Sigma(^{206}PbI^+,^{207}PbI^+,^{208}PbI^+)$; CsCl: $Cs_3Cl_2^+$; CsI: CsI^+; FA: $CH_5N_2^+$; MA: $\Sigma(CH_4^+, NH_4^+, CH_2N^+, CH_3N^+)$.

Pronounced differences in elemental distribution are observed when comparing the inorganic scaffolds prepared *via* co-deposition (Figure 5 A) and sequential deposition (Figure 5 B). Ni ($\Sigma(^{58}Ni^+,^{60}Ni^+)$) fragments from the underlying NiO_x HTL are detected in both deposition routes and serve as a positional reference. In the co-deposited inorganic scaffold, CsI (CsI^+) and CsCl ($Cs_3Cl_2^+$) fragments accumulate on the top surface and are not homogeneously distributed throughout the inorganic layer. Sequentially deposited inorganic scaffolds show the expected layering with CsCl located exclusively at the HTL interface and PbI_2-containing species ($\Sigma(^{206}PbI^+,^{207}PbI^+,^{208}PbI^+)$) found predominantly at the top surface, consistent with the process order. An additional signal of CsI at the $CsCl/PbI_2$ interface indicates a spontaneous inter diffusion process of iodide into the CsCl layer. Similarly, PbI_2-containing species accumulate both at the top and bottom of the co-deposited inorganic scaffold, possibly due to the relatively high deposition rate of PbI_2, leading to initial substrate coverage.
Counterintuitively, upon conversion to the perovskite layer (Figure 5 C/D), Cs ions appear uniformly distributed throughout the layer for both deposition routes, implying a high ionic diffusivity for Cs. The depth profiles of the PbI_2 fragments show similar trends to those observed in the initial inorganic scaffold for both deposition routes. In perovskite layers with co-deposited inorganic scaffold PbI_2 fragments tend to accumulate near the HTL-site, whereas in layers with sequentially deposited inorganic scaffold they are more concentrated at the top surface. Regardless of the deposition route, the organic fragment of FA ($CH_5N_2^+$) is homogeneously distributed throughout the perovskite layer, while MA-related fragments ($\Sigma(CH_4^+, NH_4^+, CH_2N^+, CH_3N^+)$) accumulate primarily at the top

surface. This highlights that MACl not only acts as an additive but also incorporates into the perovskite bulk, contrary to previous reports.[52–54]
To gain more insights into the distribution and diffusion of the halide components, additional measurements of the negatively charged secondary ions are performed (Figure S12). Distinct differences emerge in the iodide (I^-) and chloride (Cl^-) ion distribution when comparing the inorganic scaffolds. For the co-deposited inorganic scaffold, I ions are homogeneously distributed throughout the perovskite film. In contrast, a higher intensity of I ions is measured at the HTL site for the sequentially deposited inorganic scaffold, indicating significant ion diffusion of I into the CsCl layer, effectively forming CsI at the interface. This aligns with the detection of CsI fragments at the interface in the positive ion measurements. Cl ions tend to accumulate at both interfaces for the co-deposited inorganic scaffold but only at the bottom interface for sequential deposition, indicating reduced ion diffusion for Cl as compared to I ions. In the final perovskite films, the halide distribution is comparable for both deposition routes. Notably, I ions are homogeneously distributed throughout the layer, while Cl and Br (Br^-) ions show modest accumulation in the center of the perovskite layer.
These findings highlight that the deposition route plays a critical role in shaping the elemental distribution and ion diffusion behavior within both the inorganic scaffold and the resulting perovskite absorber. Cs ions exhibit high ion diffusivity, becoming homogeneously distributed regardless of their initial position in the inorganic scaffold. In contrast, Pb components show a lower ion diffusivity and tend to retain their original spatial distribution. The presence of CsI fragments even before thermal treatment implies a high reactivity with spontaneous reaction of the inorganic precursors. Among halide species, a lower diffusion tendency is identified for Cl and Br ions as compared to I ions.

3 Conclusion

This work introduces a fully sequential hybrid two-step deposition route – comprising the sequential deposition of CsCl and PbI_2 for the inorganic scaffold – as a viable alternative to the conventional co-deposition route, achieving comparable PCEs of 18.7% and 19.3% for wide-bandgap PSCs, respectively. While the fully sequential deposition route yields slightly reduced PCEs, gains in process effectiveness and repeatability justify the modest efficiency trade-off. Comprehensive analysis reveals distinct differences in the morphology, crystal orientation, and elemental distribution of the inorganic scaffold and perovskite thin film depending on the deposition route. Co-deposition results in a horizontal layer growth of PbI_2 platelets (out-of-plane orientation of the (001) plane), whereas sequential deposition promotes vertical growth and a secondary tilted orientation, corresponding to a preferred in-plane crystal orientation of PbI_2. The sequentially deposited inorganic scaffold exhibits an order-of-magnitude increase in surface roughness, reflecting its higher porosity compared to the co-deposited counterpart. Elemental distribution analysis reveals a pronounced layer structure for the sequentially deposited inorganic scaffold, indicating a strong dependence on the deposition route. Despite these differences in the inorganic scaffold, the resulting perovskite thin films display comparable surface morphology and only subtle variations in crystal orientation, suggesting that the initial alignment of the PbI_2 platelets plays a templating role during perovskite formation. Elemental distribution analysis indicates high ion diffusivity for Cs, I and FA ions, which are homogeneously distributed throughout the final perovskite thin film. In contrast, Pb and Cl ions are less diffusive, with spatial distributions largely retained from the initial inorganic scaffold. Overall, this work reveals the influence of the deposition route on the inorganic scaffold in hybrid two-step perovskite fabrication. A deeper understanding of the interplay between morphology, crystal growth orientation and elemental diffusion is essential to further optimize process stability, film quality, and ultimately device performance. Our findings position the sequential deposition route of the inorganic scaffold as a viable route toward

industrial PSC production.

4 Experimental Section

Materials

[2-(9H-carbazol-9-yl)ethyl]phosphonic acid (2PACz: TCI, CAS: 20999-38-6), Lead iodide (PbI_2: TCI, 99.99%, trace metals basis, CAS: 10101-63-0), Formamidinium iodide (FAI: Greatcell solar materials, CAS: 879643-71-7), Formamidinium bromide (FABr: Dyenamo, CAS: 146958-06-7), Methylammonium chloride (MACl: Dyenamo, CAS: 593-51-1), Cesium chloride (CsCl: TCI, ≥99.0% (titration), CAS: 7647-17-8), Fullerene-C_{60} (C_{60}: Sigma-Aldrich, CAS: 99685-96-8), Bathocuproine (BCP: Lumtec, CAS: 4733-39-5), n-Butylammonium iodide (BAI: Greatcell solar materials, CAS: 36945-08-1), Propane-1,3-diammonium iodide ($PDAI_2$: Greatcell solar materials, CAS: 120675-53-8). Ethanol absolute anhydrous, ≥ 99.8%, (EtOH, CAS: 64-17-5) was ordered from VWR Chemicals.

Device Fabrication

Single-Junction (SJ) Perovskite Solar Cells

The planar *p-i-n* PSCs with the layer stack glass/ITO/NiO_x/2PACz/perovskite/ $PDAI_2$+BAI/C_{60}/BCP/Ag were fabricated as follows.

Sample preparation and cleaning: The glass substrates with 120 nm thick indium tin oxide (ITO) coating (sheet resistance 15 Ωcm^{-2}, Luminescence Technology, CAS: 50926-11-9) were cut in 16 mm × 16 mm and subsequently cleaned in an ultrasonic bath with acetone and isopropanol for 20 min each. This was followed by 5 min of oxygen plasma treatment before the deposition of the hole transport (HTL) layer.

Hole transport layer (HTL): For the HTL layer, a 5 nm thick NiO_x film was sputtered from a NiO_x target (4 inch, 99.99% pure, Kurt J. Lesker Company) using 100 W power (7.95 W in^{-2} power density) in a gas mixture of Ar and O_2 at 1 mTorr on the ITO substrate with a fixed flow rate of 0.2 sccm for O_2 and a variable flow rate of Ar to achieve the set pressure. Then, a thin layer of 2PACz was deposited on the ITO/NiO_x substrate by dispensing 75 µL 2PACz solution (0.5 mg mL^{-1} in anhydrous EtOH) on the substrate with a resting time of 5 s followed by rotation at 3000 rpm for 30 s. The substrates were then annealed at a temperature of 100 °C for 10 min. A second washing step was used to remove any unbound molecules. Here, 150 µL of pure EtOH was used which was dynamically dispensed onto the substrate within 2 s at 3000 rpm for 30 s of total rotation time. The substrates were then annealed at 100 °C for 10 minutes.

Perovskite deposition: Vacuum-based deposition of perovskite precursor materials was performed using a PEROvap system (M.Braun Inertgas-Systeme GmbH Dresden) integrated into a nitrogen glovebox. Individual quartz crystal microbalances (QCMs) were used to measure the rate of each material. A cooling inner surface, surrounding all sublimation sources, was set to −20 °C. Prior to the heating process, the system was evacuated, with a standard base pressure at start of heating of $< 3x10^{-6}$ mbar. For each process, the sublimation rates were kept constant in an automated process. The substrate temperature (18 °C) was kept constant for all experiments. Source to substrate setup uses a 300 mm vertical distance and 165 mm lateral distance between the sublimation source and the substrate. Static deposition rates of 1.0 and 0.1 $Å s^{-1}$ of PbI_2 and CsCl, respectively, were used for both sequential and co-deposition of the inorganic scaffold. In the case of co-deposition, a film thickness of 300 nm was set as the final film thickness for PbI_2, terminating the deposition. The final thickness of CsCl was 30 ± 2 nm. For sequential deposition, first 30 nm of CsCl were deposited, followed by 300 nm of PbI_2. For all experiments, cylindrical crucibles with a volume of 10 cm^3 were used with material filling of 5 g for PbI_2 and CsCl.

Organic cation solution deposition: Organic cation solution was deposited *via* a spin-coating process. A solution of FAI (35%), FABr (65%) in anhydrous EtOH was prepared with MACl added as an additive with a ratio of 10%mol relative to the total amount of FA^+.[31, 33] 100 µL of the organic cation solution was dispensed dynamically at a rotation speed of 4000 rpm for 30 seconds. The substrates were then annealed at 150 °C for 20 min under ambient conditions at a relative humidity of 30-40%. The spin-coating process took place in a N_2-filled glovebox.

Surface passivation: A solution of $PDAI_2$ and BAI was prepared according to Pappenberger *et al.* by first dissolving 4 mg of $PDAI_2$ under heating in anhydrous EtOH to 50 °C.[55] The solution was then transferred to a second vial containing 4 mg of BAI. The solution was agitated using a vortex mixer to yield a stock solution of 1 mg mL^{-1} related to the content of $PDAI_2$. The stock solution was diluted to a concentration of 0.3 mg mL^{-1} with addition of pure EtOH. For application of the surface passivation, 100 µL of the diluted solution was dispensed on the substrate with a resting time of 5 s followed by rotation at 4500 rpm for 30 s. The substrates were then annealed at 100 °C for 10 min.

Electron transport layer (ETL) and top contact: As electron transport (ETL) layer, 20 nm of C_{60} and 5 nm of BCP were thermally evaporated and deposited using an Angstrom evaporation system at an evaporation rate of 0.1-0.2 Å s^{-1} at a pressure of around 10^{-6} mbar. Subsequently, 100 nm Ag was thermally evaporated using a shadow mask to define the active area to 10.5 mm^2 and complete the PSCs with 4 pixels per substrate.

Device Characterization

Current Density-Voltage (*J*–*V*) Measurements

The *J*–*V* characteristics of the SJ PSCs were measured with a class AAA xenon-lamp solar simulator (Newport Oriel Sol3A) with a scan rate set at 0.6 V s^{-1} using a sourcemeter (Keithley 2400) with an air-mass 1.5 global (AM1.5G) spectra (100 mW cm^{-2}). The solar simulator irradiation intensity was calibrated using a certified Si solar cell (Fraunhofer ISE, calibrated 2025) equipped with a KG5 band pass filter (Schott). The device parameters of the light-soaked PSCs were used for the results. The stabilized PCE of the PSCs was determined by measuring the photocurrent at the maximum power point (MPP) for 300 s by using a perturb and observing algorithm under continuous AM 1.5G illumination. The measurement was performed in a N_2-filled glovebox. No shadow mask was used for the measurement.

External Quantum Efficiency (EQE)

The EQE was measured using a PVE300 photovoltaic QE system (Bentham EQE system). A chopping frequency in the range of 560-590 Hz with an integration time of 500 ms was used to acquire the spectra in a wavelength range from 300-850 nm. An illumination spot (0.74 mm) was utilized to obtain the average over possible variations in the EQE spectra. The bandgap of all processed perovskite thin films is determined based on the differential of the EQE curves near the absorption edge (maximum of d(EQE)/d(E)) according to Krückemeier et al.[56].

Scanning Electron Microscopy (SEM)

Field emission top-view SEM images were taken with a scanning electron microscope (Zeiss LEO Gemini 1530) with an in-lens detector and a aperture size of 20-30 µm. For cross-sectional analyses, the cross sections were covered with a 3 nm thick platinum layer

deposited by sputtering to prevent charging. The applied acceleration voltages for surface and cross sectional analyses range between 5-10 kV.

Atomic Force Microscopy (AFM)

AFM images were obtained using a Nano Wizard II (JPK Instruments). The scanning area was 5 µm × 5 µm. For each parameter, 2-3 measurements were conducted, and the average root-mean-square (RMS) value was determined.

UV-Vis Spectrophotometry (UV)

Transmittance and reflectance spectra of the perovskite thin films were measured using a PerkinElmer Lambda1050 spectrophotometry setup equipped with a double-monochromator and a modulated source. A chopper frequency of 46 Hz was applied.

Confocal Scanning Microscopy

Confocal scanning microscopy measurements were performed with a MarSurf3D system.

PicoDrop Deposition

Droplets of the organic cation solution were applied with the PicoDrop kit. Hereby, cartridges which jet 30 pL droplets were used. The organic cation solution with optimal molarity was used in each case.

X-Ray Diffraction (XRD)

X-Ray diffraction measurements of the inorganic scaffolds and perovskite thin-films were performed using a Bruker D2 Phaser system with Cu-K_α radiation (λ = 1.5405 Å) in Bragg–Brentano configuration using a LynxEye detector. The diffraction pattern was measured for half-stacks with an architecture of glass/ITO/NiO_x/2PACz/perovskite to obtain comparable perovskite nucleation and crystallinity as in the actual device architecture.

Grazing-Incidence Wide-Angle X-Ray Scattering (GIWAXS)

The GIWAXS measurements were carried out on a Bruker D8 Advance equipped with a Cu X-ray source (40 kV, 40 mA), a Goebel mirror, a 0.5 mm micro mask and a 0.3 mm snout on the primary track and an Eiger2 R 500K 2D detector on the secondary track. The incidence angle was fixed at 1.5°. First, all acquired images were projected onto a virtual detector directly behind the real goniometer circle using a home-developed program in MATLAB.[57] For reshaping the experimentally acquired data into 2D diffractograms in reciprocal space, the open-access software GIXSGUI was used.[58]

Time-of-Flight Secondary Ion Mass Spectrometry (ToF-SIMS)

Time-of-Flight Secondary Ion Mass Spectrometry, (ToF-SIMS), was performed on a TOF.SIMS5 instrument (ION-TOF GmbH, Münster, Germany) equipped with a Bi cluster primary ion source and a reflectron type time-of-flight analyzer. UHV base pressure during analysis was $< 7\times10^{-8}$ mbar. For high mass resolution the Bi source was operated in the "high current bunched" mode providing short Bi_3^+ primary ion pulses at 25 keV energy, a lateral resolution of approx. 4 µm, and a target current of 0.31 - 0.35 pA at 10 kHz repetition rate. The short pulse length of 1.5 ns allowed for high mass resolution (6500 m/Δm for $^{208}Pb^+$). The primary ion beam was rastered across a 200×200 μm^2 field of view on the sample, and 128×128 data points were recorded. Mass scale calibrations were based on Li^+, Na^+, $^{204}Pb^+$, $^{206}Pb^+$, Cs_2^+, and $^{37}Cl^-$, PO_2^-, CsI_2^-, PbI_2^-, respectively. For depth

profiling a dual beam analysis in interlaced mode was performed. For both secondary ion polarities, the sputter gun for depth profiling was operated with Ar^+_{1500} ions, 10 keV, scanned over a concentric field of 500×500 µm^2, (target current 7.4 - 7.5 nA). The applied sputter ion fluence was used as an arbitrary measure for depth. Note, however, that this scale might not be linear due to different erosions speeds of the different deposited layers. Secondary ion intensities are plotted normalized to their maximum intensities each, yielding more noise for weaker absolute intensities. It was ensured that signals showing SI detector saturation were omitted.

Statistical Analysis

To check the deviation of the statistical results from each other, *Welch's t test* was applied. *Welch's t test* is an adaption of the *Student's t* test and is more reliable when the two samples have unequal variances and possibly unequal sample sizes.[59–61] These tests are often referred to as "independent samples" or "unpaired" t tests because they are usually applied when the statistics underlying the two samples being compared do not overlap. It is assumed that the sample means for the two samples being compared are normally distributed.[59]
The t statistic for testing whether the results differ from each other or not can be calculated as follows:

$$t = \frac{\overline{X} - \overline{Y}}{\sqrt{\frac{S_x^2}{n_x} + \frac{S_y^2}{n_y}}}, \tag{1}$$

whereas $\overline{X}$ and $\overline{Y}$ are the mean values, S_x and S_y the standard deviations and n_x and n_y the sample sizes.

Acknowledgements

This work was partly carried out with the support of the Karlsruhe Nano Micro Facility (KNMFi) (www.kit.edu/knmf), a Helmholtz Research Infrastructure at Karlsruhe Institute of Technology (KIT) within the project 2024-033-032255. The assistance of Richard Thelen with confocal scanning microscopy measurements within the KMNFi project 2025-033-032285 is acknowledged. Financial support by the Initiating and Networking funding of the Helmholtz Association (Project Zeitenwende and the Solar Technology Acceleration Platform (Solar TAP)), by the Ministry of Science and Culture in the State of Lower Saxony through the program "zukunft.niedersachsen" (project NextGenPV), by the program oriented funding IV of the Helmholtz Association (Materials and Technologies for the Energy Transition, Topic 1: Photovoltaics and Wind Energy, Code: 38.01.03), and the German Federal Ministry for Economic Affairs and Climate Action (BMWK) through the SHAPE project (03EE1123 A-E) is greatly acknowledged. We acknowledge support by the Karlsruhe School of Optics & Photonics (KSOP) and the Ministry of Science, Research and Arts of Baden-Württemberg as part of the sustainability financing of the projects of the Excellence Initiative II. This work was partially funded by the European Union. Views and opinions expressed are however those of the author(s) only and do not necessarily reflect those of the European Union or RIA. Neither the European Union nor the granting authority can be held responsible for them. The NEXUS project has received funding from the European Union's Horizon Europe research and innovation program under grant agreement No. 101075330. The authors thank the whole "Perovskite Taskforce" at KIT for fruitful discussions and assistance.

Authors Contribution

Julian Petry: Conceptualization, Formal analysis, Investigation (Lead), Data Curation (Lead), Writing - Original Draft, Visualization, Project administration. **Ronja Pappenberger:** Conceptualization, Formal analysis, Investigation (Lead), Data Curation (Lead), Writing - Original Draft, Visualization, Project administration. **Alexander Welle:** Investigation (ToF-SIMS), Data Curation (Supporting), Writing - Review & Editing. **Tonghan Zhao:** Investigation (GIWAXS), Data Curation (Supporting), Writing - Review & Editing. **Alexander Diercks:** Investigation (SEM), Writing - Review & Editing. **Raphael Pesch:** Investigation (PicoDrop), Writing - Review & Editing. **Paul Fassl:** Conceptualization (Supporting), Writing - Review & Editing, Supervision, Funding acquisition. **Ulrich W. Paetzold:** Conceptualization (Supporting), Writing - Review & Editing, Supervision, Funding acquisition.

Declaration of Interests

The authors declare no competing interests.

Data Availability Statement

The data that support the findings of this study are available from the corresponding author upon reasonable request. The data supporting this article has been included as part of the ESI. The data generated during and/or analyzed during the current study has been deposited at the KITopen repository under a CC-BY 4.0 Creative Commons Attribution license: KITopen (2025), **DOI will be added upon acceptance**.

References

[1] A. Kojima et al. "Organometal Halide Perovskites as Visible-Light Sensitizers for Photovoltaic Cells". In: *Journal of the American Chemical Society* 131.17 (2009), pp. 6050–6051. DOI: 10.1021/ja809598r.

[2] N. R. E. Laboratory. *Best Research-Cell Efficiency Chart*. https://www.nrel.gov/pv/cell-efficiency.html. accessed: July, 2025.

[3] T. Niewelt et al. "Reassessment of the intrinsic bulk recombination in crystalline silicon". In: *Sol. Energy Mater. Sol. Cells* 235, (2022), p. 111467. DOI: 10.1016/j.solmat.2021.111467.

[4] E. Aydin et al. "Pathways toward commercial perovskite/silicon tandem photovoltaics". In: *Science* 383.6679 (2024), eadh3849. DOI: 10.1126/science.adh3849.

[5] J. Liu et al. "Perovskite/silicon tandem solar cells with bilayer interface passivation". In: *Nature* 635.8039 (2024), pp. 596–603. DOI: 10.1038/s41586-024-07997-7.

[6] L. Jia et al. "Efficient perovskite/silicon tandem with asymmetric self-assembly molecule". In: *Nature* (2025), pp. 1–3. DOI: 10.1038/s41586-025-09333-z.

[7] A. Bhambhani. *Record 31.1% efficiency for Trinasolar's tandem solar cell*. https://taiyangnews.info/technology/311-efficiency-perovskite-silicon-tandem-cell-trinasolar. 2025.

[8] F. Fu et al. "Monolithic Perovskite-Silicon Tandem Solar Cells: From the Lab to Fab?" In: *Advanced Materials* 34.24 (2022), p. 2106540. DOI: 10.1002/adma.202106540.

[9] S. Bächle and A. Kraft. *Oxford PV and Fraunhofer ISE develop full-sized tandem PV module with record efficiency of 25 percent*. https://www.ise.fraunhofer.de/en/press-media/press-releases/2024/oxford-pv-and-fraunhofer-ise-develop-full-sized-tandem-pv-module-with-record-efficiency-of-25-percent.html. 2024.

[10] L. Duan et al. "Stability challenges for the commercialization of perovskite-silicon tandem solar cells". In: *Nature Reviews Materials* 8.4 (2023), pp. 261–281. DOI: 10.1038/s41578-022-00521-1.

[11] F. E. Subhan et al. "Optical optimization of double-side-textured monolithic perovskite–silicon tandem solar cells for improved light management". In: *RSC Adv.* 10, (2020), pp. 26631–26638. DOI: 10.1039/d0ra04634e.

[12] M. De Bastiani et al. "Efficient bifacial monolithic perovskite/silicon tandem solar cells via bandgap engineering". In: *Nat. Energy* 6, (2021), pp. 167–175. DOI: 10.1038/s41560-020-00756-8.

[13] F. Gota et al. "Energy yield modelling of textured perovskite/silicon tandem photovoltaics with thick perovskite top cells". In: *Opt. Express* 30, (2022), p. 14172. DOI: 10.1364/oe.447069.

[14] W. Qarony et al. "Influence of Perovskite Interface Morphology on the Photon Management in Perovskite/Silicon Tandem Solar Cells". In: *ACS Appl. Mater. Interfaces* 12, (2020), pp. 15080–15086. DOI: 10.1021/acsami.9b21985.

[15] A. S. Subbiah et al. "High-Performance Perovskite Single-Junction and Textured Perovskite/Silicon Tandem Solar Cells via Slot-Die-Coating". In: *ACS Energy Lett.* 5, (2020), pp. 3034–3040. DOI: 10.1021/acsenergylett.0c01297.

[16] F. H. Isikgor et al. "Concurrent cationic and anionic perovskite defect passivation enables 27.4% perovskite/silicon tandems with suppression of halide segregation". In: *Joule* 5, (2021), pp. 1566–1586. DOI: 10.1016/j.joule.2021.05.013.

[17] F. Sahli et al. “Fully textured monolithic perovskite/silicon tandem solar cells with 25.2% power conversion efficiency”. In: *Nature Materials* 17.9 (2018), pp. 820–826. DOI: 10.1038/s41563-018-0115-4.

[18] M. Jošt et al. “21.6%-Efficient Monolithic Perovskite/Cu(In,Ga)Se2 Tandem Solar Cells with Thin Conformal Hole Transport Layers for Integration on Rough Bottom Cell Surfaces”. In: *ACS Energy Letters* 4.2 (2019), pp. 583–590. DOI: 10.1021/acsenergylett.9b00135.

[19] Y. Vaynzof. “The Future of Perovskite Photovoltaics–Thermal Evaporation or Solution Processing?” In: *Advanced Energy Materials* 10.48 (2020). DOI: 10.1002/aenm.202003073.

[20] L. Gil-Escrig et al. “Vacuum Deposited Triple-Cation Mixed-Halide Perovskite Solar Cells”. In: *Advanced Energy Materials* 8.14 (2018). DOI: 10.1002/aenm.201703506.

[21] T. Abzieher et al. “Efficient All-Evaporated pin-Perovskite Solar Cells: A Promising Approach Toward Industrial Large-Scale Fabrication”. In: *IEEE Journal of Photovoltaics* 9.5 (2019), pp. 1249–1257. DOI: 10.1109/jphotov.2019.2920727.

[22] C. Momblona et al. “Efficient methylammonium lead iodide perovskite solar cells with active layers from 300 to 900 nm”. In: *APL Materials* 2.8 (2014). DOI: 10.1063/1.4890056.

[23] L. Cojocaru et al. “Detailed Investigation of Evaporated Perovskite Absorbers with High Crystal Quality on Different Substrates”. In: *ACS Applied Materials & Interfaces* 10.31 (2018), pp. 26293–26302. DOI: 10.1021/acsami.8b07999.

[24] M. Roß et al. “Co-Evaporated Formamidinium Lead Iodide Based Perovskites with 1000 h Constant Stability for Fully Textured Monolithic Perovskite/Silicon Tandem Solar Cells”. In: *Advanced Energy Materials* 11.35 (2021). DOI: 10.1002/aenm.202101460.

[25] M. Kroll et al. “Insights into the evaporation behaviour of FAI: material degradation and consequences for perovskite solar cells”. In: *Sustainable Energy Fuels* 6 (13 2022), pp. 3230–3239. DOI: 10.1039/D2SE00373B.

[26] J. Borchert et al. “Impurity Tracking Enables Enhanced Control and Reproducibility of Hybrid Perovskite Vapor Deposition”. In: *ACS Applied Materials & Interfaces* 11.32 (2019). PMID: 31314481, pp. 28851–28857. DOI: 10.1021/acsami.9b07619.

[27] I. Levchuk et al. “Deciphering the Role of Impurities in Methylammonium Iodide and Their Impact on the Performance of Perovskite Solar Cells”. In: *Advanced Materials Interfaces* 3.22 (2016), p. 1600593. DOI: 10.1002/admi.201600593.

[28] K. P. S. Zanoni et al. “Photovoltaic Devices Using Sublimed Methylammonium Lead Iodide Perovskites: Long-Term Reproducible Processing”. In: *Solar RRL* 7.7 (2023), p. 2201073. DOI: 10.1002/solr.202201073.

[29] J. Petry et al. “Industrialization of perovskite solar cell fabrication: strategies to achieve high-throughput vapor deposition processes”. In: *EES Sol.* 1 (3 2025), pp. 404–418. DOI: 10.1039/D5EL00069F.

[30] P. S. Schulze et al. “Perovskite hybrid evaporation/spin coating method: From band gap tuning to thin film deposition on textures”. In: *Thin Solid Films* 704 (2020), p. 137970. DOI: 10.1016/j.tsf.2020.137970.

[31] Y. Li et al. “Wide Bandgap Interface Layer Induced Stabilized Perovskite/Silicon Tandem Solar Cells with Stability over Ten Thousand Hours”. In: *Advanced Energy Materials* 11.48 (2021), p. 2102046. DOI: 10.1002/aenm.202102046.

[32] X. Luo et al. “Efficient Perovskite/Silicon Tandem Solar Cells on Industrially Compatible Textured Silicon”. In: *Advanced Materials* 35.9 (2023), p. 2207883. DOI: 10.1002/adma.202207883.

[33] O. Er-raji et al. “Insights into Perovskite Film Formation Using the Hybrid Evaporation/Spin-Coating Route: An In Situ XRD Study”. In: *ACS Applied Energy Materials* 6.11 (2023), pp. 6183–6193. DOI: 10.1021/acsaem.3c00698.

[34] O. Er-raji et al. “Tailoring perovskite crystallization and interfacial passivation in efficient, fully textured perovskite silicon tandem solar cells”. In: *Joule* 8.10 (2024), pp. 2811–2833. DOI: 10.1016/j.joule.2024.06.018.

[35] O. Er-raji et al. “Loss Analysis of Fully-Textured Perovskite Silicon Tandem Solar Cells: Characterization Methods and Simulation toward the Practical Efficiency Potential”. In: *Solar RRL* 7.24 (2023), p. 2300659. DOI: 10.1002/solr.202300659.

[36] A. Z. Afshord et al. “Efficient and Stable Inverted Wide-Bandgap Perovskite Solar Cells and Modules Enabled by Hybrid Evaporation-Solution Method”. In: *Advanced Functional Materials* 33.31 (2023), p. 2301695. DOI: 10.1002/adfm.202301695.

[37] O. Er-raji et al. “Toward efficient and industrially compatible fully textured perovskite silicon tandem solar cells: Controlled process parameters for reliable perovskite formation”. In: *Progress in Photovoltaics: Research and Applications* 33.1 (2025), pp. 86–99. DOI: 10.1002/pip.3770.

[38] Q. Xu et al. “Diffusible Capping Layer Enabled Homogeneous Crystallization and Component Distribution of Hybrid Sequential Deposited Perovskite”. In: *Advanced Materials* 36.5 (2024), p. 2308692. DOI: 10.1002/adma.202308692.

[39] A. Ullah et al. “Improved Crystallinity and Efficiency in Perovskite Solar Cells through Layered Hybrid Deposition”. In: *ACS Energy Letters* 10.1 (2025), pp. 30–33. DOI: 10.1021/acsenergylett.4c02797.

[40] X. Y. Chin et al. “Interface passivation for 31.25%-efficient perovskite/silicon tandem solar cells”. In: *Science* 381.6653 (2023), pp. 59–63. DOI: 10.1126/science.adg0091.

[41] Z. Liu et al. “Strained heterojunction enables high-performance, fully textured perovskite/silicon tandem solar cells”. In: *Joule* 8.10 (2024), pp. 2834–2850. DOI: 10.1016/j.joule.2024.06.015.

[42] O. Er-raji et al. “Coating dynamics in two-step hybrid evaporated/blade-coated perovskites for scalable fully-textured perovskite/silicon tandem solar cells”. In: *EES Sol.* 1 (3 2025), pp. 419–430. DOI: 10.1039/D5EL00073D.

[43] Q. Luo et al. “Combined evaporation-solution methodology for high-efficiency perovskite solar cells with exceptional reproducibility”. In: *Journal of Materials Chemistry A* (2025). DOI: 10.1039/d5ta03304g.

[44] L. Mao et al. “Fully Textured, Production-Line Compatible Monolithic Perovskite/Silicon Tandem Solar Cells Approaching 29% Efficiency”. In: *Advanced Materials* 34.40 (2022), p. 2206193. DOI: 10.1002/adma.202206193.

[45] X. Zheng et al. “Solvent engineering for scalable fabrication of perovskite/silicon tandem solar cells in air”. In: *Nature Communications* 15.1 (2024). DOI: 10.1038/s41467-024-49351-5.

[46] R. Pesch et al. “Hybrid Two-Step Inkjet-Printed Perovskite Solar Cells”. In: *Solar RRL* 8.13 (2024), p. 2400165. DOI: 10.1002/solr.202400165.

[47] J. A. Steele et al. “How to GIWAXS: Grazing Incidence Wide Angle X-Ray Scattering Applied to Metal Halide Perovskite Thin Films”. In: *Advanced Energy Materials* 13.27 (2023). DOI: 10.1002/aenm.202300760.

[48] K. Meng et al. “In Situ Observation of Crystallization Dynamics and Grain Orientation in Sequential Deposition of Metal Halide Perovskites”. In: *Advanced Functional Materials* 29.35 (2019). DOI: 10.1002/adfm.201902319.

[49] A. Diercks et al. “Sequential Evaporation of Inverted FAPbI3 Perovskite Solar Cells – Impact of Substrate on Crystallization and Film Formation”. In: *ACS Energy Letters* 10.3 (2025), pp. 1165–1173. DOI: 10.1021/acsenergylett.4c03315.

[50] T. M. Brenner et al. “Conversion of single crystalline PbI2 to CH3NH3PbI3: Structural relations and transformation dynamics”. In: *Chemistry of Materials* 28.18 (2016), pp. 6501–6510. DOI: 10.1021/acs.chemmater.6b01747.

[51] S. Kumar et al. “Topotactic, vapor-phase, in situ monitored formation of ultrathin, phase-pure 2D-on-3D halide perovskite surfaces”. In: *ACS applied materials & interfaces* 15.19 (2023), pp. 23908–23921. DOI: 10.1021/acsami.3c01881.

[52] M. A. A. Mahmoud et al. “Tuning Perovskite Crystal Growth Dynamics Using Additives on Textured Silicon Substrates”. In: *Solar RRL* 8.24 (2024). DOI: 10.1002/solr.202400471.

[53] M. M. Tavakoli et al. “Synergistic Crystal and Interface Engineering for Efficient and Stable Perovskite Photovoltaics”. In: *Advanced Energy Materials* 9.1 (2018). DOI: 10.1002/aenm.201802646.

[54] M. M. Byranvand and M. Saliba. “Defect Passivation of Perovskite Films for Highly Efficient and Stable Solar Cells”. In: *Solar RRL* 5.8 (2021). DOI: 10.1002/solr.202100295.

[55] R. Pappenberger et al. “Versatile Two-Step Process for Perovskite-Based Tandem Photovoltaics”. In: *Solar RRL* 9.13 (2025). DOI: 10.1002/solr.202500193.

[56] L. Krückemeier et al. “How to Report Record Open-Circuit Voltages in Lead-Halide Perovskite Solar Cells”. In: *Advanced Energy Materials* 10.1 (2020), p. 1902573. DOI: 10.1002/aenm.201902573.

[57] J. C. Fischer et al. “GIWAXS Characterization of Metal-Organic Framework Thin Films and Heterostructures: Quantifying Structure and Orientation”. In: *Advanced Materials Interfaces* 10.11 (2023). DOI: 10.1002/admi.202202259.

[58] Z. Jiang. “GIXSGUI: a MATLAB toolbox for grazing-incidence X-ray scattering data visualization and reduction, and indexing of buried three-dimensional periodic nanostructured films”. In: *Journal of Applied Crystallography* 48.3 (2015), pp. 917–926. DOI: 10.1107/s1600576715004434.

[59] B. L. Welch. “THE GENERALIZATION OF ‘STUDENT’S’ PROBLEM WHEN SEVERAL DIFFERENT POPULATION VARLANCES ARE INVOLVED”. In: *Biometrika* 34, (1947), pp. 28–35. DOI: 10.1093/biomet/34.1-2.28.

[60] G. D. Ruxton. “The unequal variance t-test is an underused alternative to Student’s t-test and the Mann–Whitney U test”. In: *Behav. Ecol.* 17, (2006), pp. 688–690. DOI: 10.1093/beheco/ark016.

[61] B. Derrick and P. White. “Why Welch’s test is Type I error robust”. In: *Quant. Meth. Psych.* 12, (2016), pp. 30–38. DOI: 10.20982/tqmp.12.1.p030.

[62] Dotmatics. *GraphPad: T Test Calculator*. https://www.graphpad.com/quickcalcs/ttest1/?format=C. accessed: July, 2025.

Supporting Information

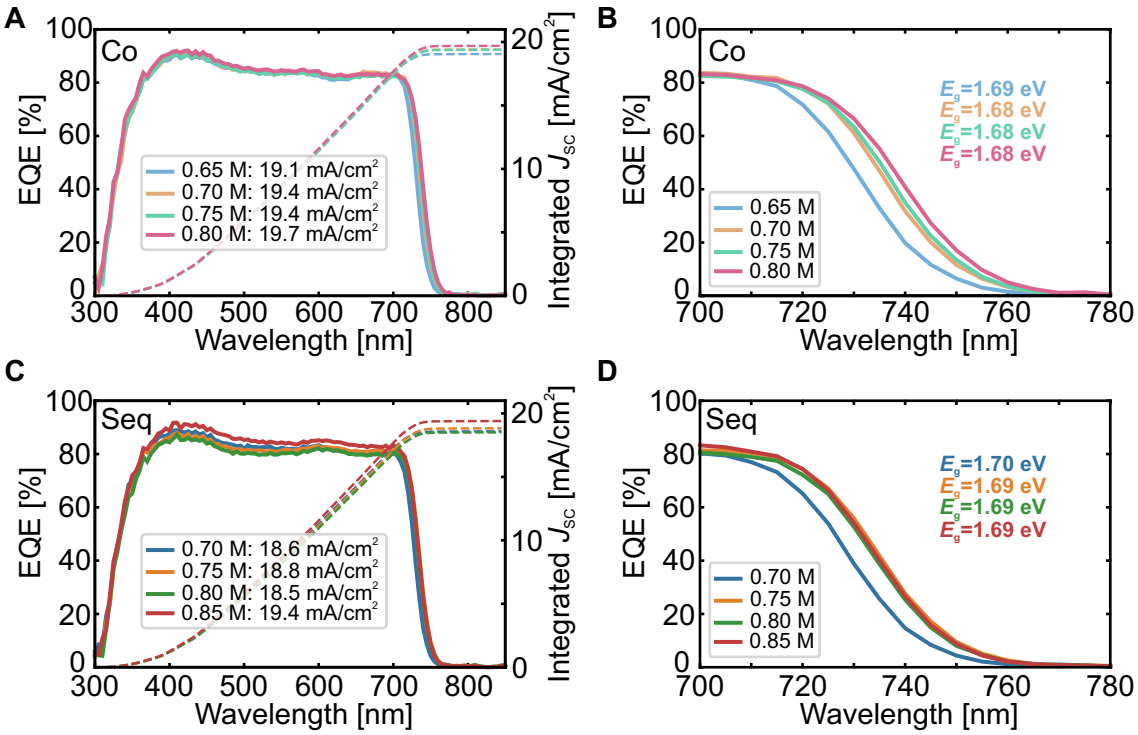

Figure S1: EQE spectra for different molarities of the organic cation solution for **A** co-deposition (Co) and **C** sequential deposition (Seq) of the inorganic scaffold. Optical bandgap extracted from the inflection point of the EQE spectra for **B** co-deposition (Co) and **D** sequential deposition (Seq) of the inorganic scaffold.

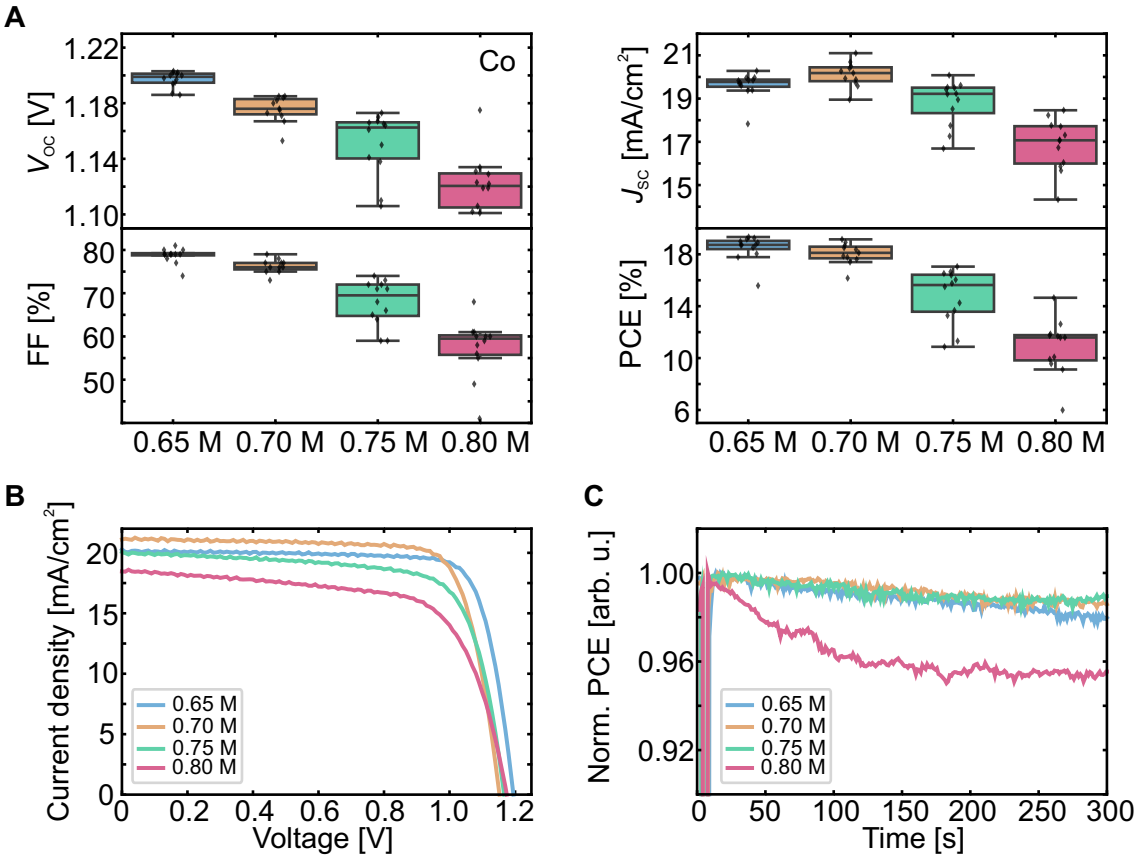

Figure S2: **A** Statistical distribution (in total 47 devices) of the open-circuit voltage (V_{OC}), fill factor (FF), short-circuit current density (J_{SC}) and power conversion efficiency (PCE), **B** current density *versus* voltage (J-V) characteristics and **C** maximum power point (MPP) tracking for different molarities of the organic cation solution for co-deposition (Co) of the inorganic scaffold.

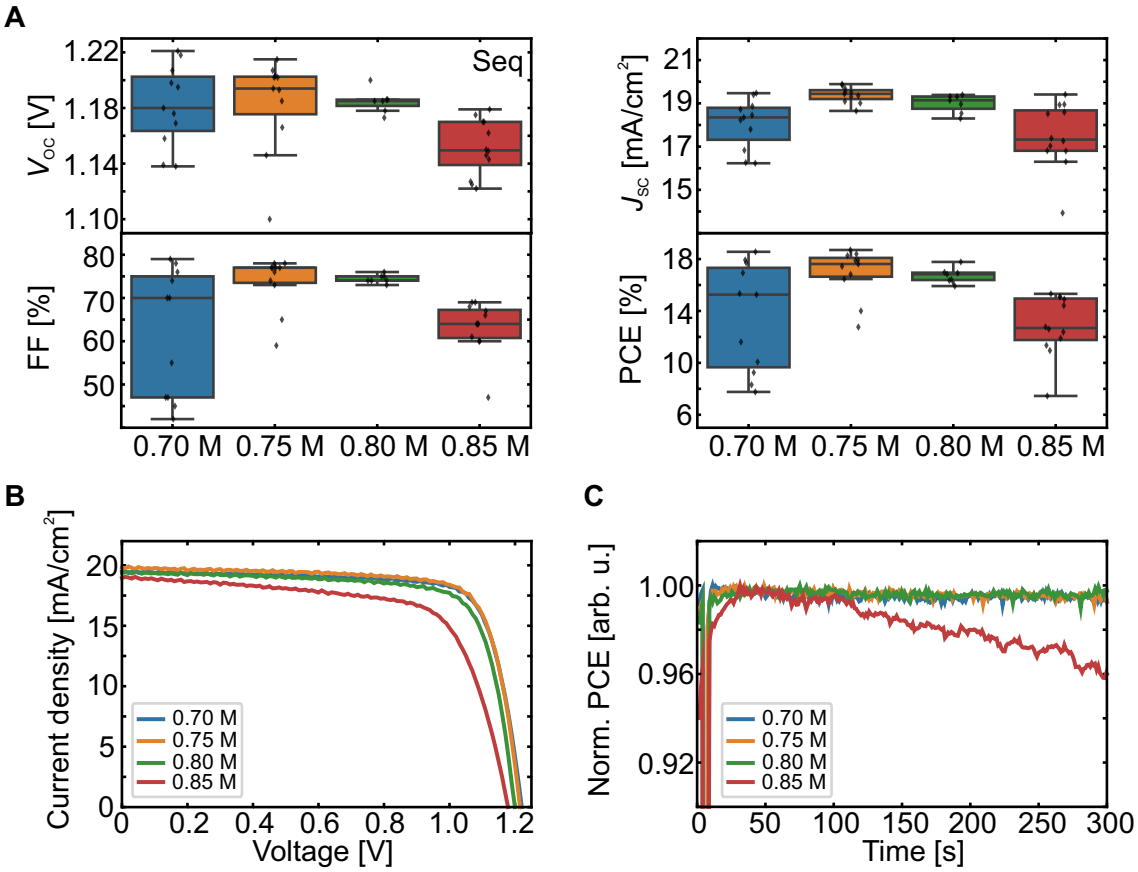

Figure S3: **A** Statistical distribution (in total 42 devices) of the open-circuit voltage (V_{OC}), fill factor (FF), short-circuit current density (J_{SC}) and power conversion efficiency (PCE), **B** current density *versus* voltage (J-V) characteristics and **C** maximum power point (MPP) tracking for different molarities of the organic cation solution for sequential deposition (Seq) of the inorganic scaffold.

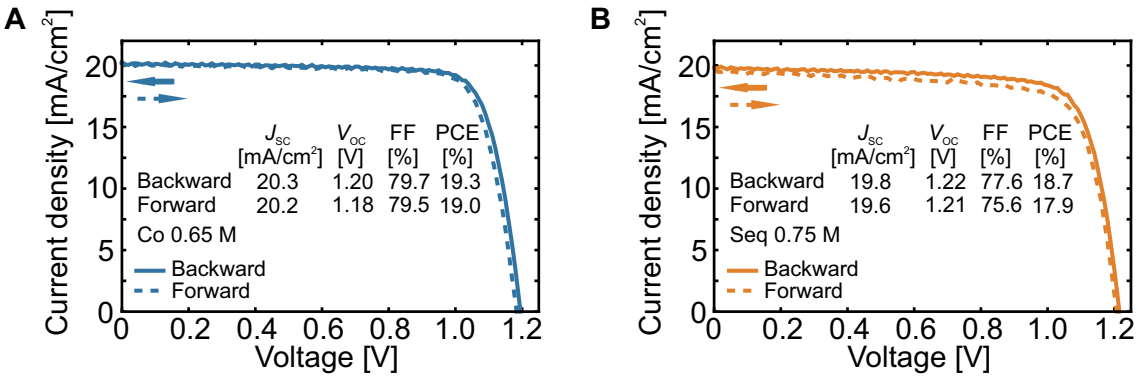

Figure S4: Current density *versus* voltage (J-V) characteristics of the champion opaque PSCs with **A** co-deposition (Co) and **B** sequential deposition (Seq) of the inorganic scaffold with optimal molarity of the organic cation solution.

Table S1: Photovoltaic parameters of the champion opaque PSCs with co-deposition (Co) and sequential deposition (Seq) of the inorganic scaffold with optimal molarity of the organic cation solution.

samples	scan direction	V_{OC} [V]	J_{SC} [mA cm^{-2}]	FF [%]	PCE [%]	HI [%][a]
Co 0.65 M	backward	1.20	20.28	79.74	19.33	1.91
	forward	1.18	20.15	79.50	18.96	
Seq 0.75 M	backward	1.22	19.83	77.64	18.70	4.28
	forward	1.21	19.60	75.63	17.90	

[a)] Note: HI [%] = [(PCE at backward scan - PCE at forward scan)/PCE at backward scan] · 100.

Table S2: *Welch's t test* results for the backward PCE, V_{OC}, J_{SC} and FF parameters of the opaque PSCs with co-deposition (Co) and sequential deposition (Seq) of the inorganic scaffold with optimal molarity of the organic cation solution. The calculation was performed using a *t test* calulator.[62]

parameter	samples	P-value	interpretation difference
PCE	Co and Seq	0.0296	statistically significant
V_{OC}	Co and Seq	0.2036	not statistically significant
J_{SC}	Co and Seq	0.3078	not statistically significant
FF	Co and Seq	0.0262	statistically significant

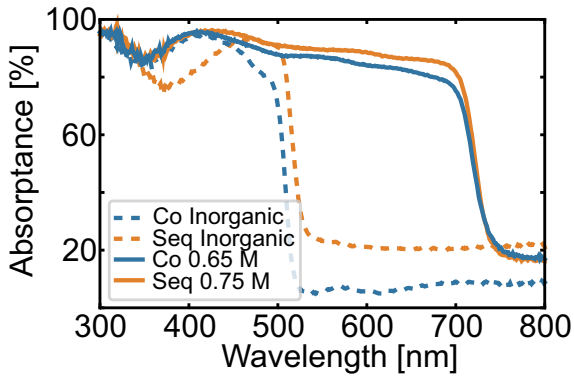

Figure S5: Absorptance spectra for the inorganic scaffold as well as the perovskite films with optimal molarity of the organic cation solution fabricated with co-deposition (Co) and sequential deposition (Seq) of the inorganic scaffold.

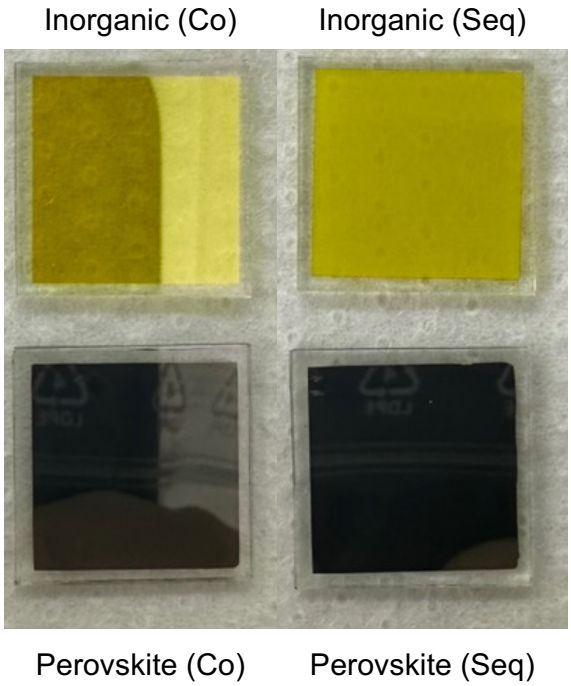

Figure S6: Optical photographies of the inorganic scaffolds and the corresponding perovskite films for co-deposition (Co) and sequential deposition (Seq). For the perovskite films, the optimal molarity of the organic cation solution is used.

Table S3: Surface profilometry of the inorganic scaffold and final perovskite layers with co-deposition (Co) and sequential deposition (Seq) of the inorganic scaffold. For the perovskite films, the optimal molarity of the organic cation solution is used.

deposition route	layer	thickness [nm]
Co	inorganic	325 ± 4
Seq	inorganic	409 ± 4
Co	perovskite	524 ± 4
Seq	perovskite	682 ± 5

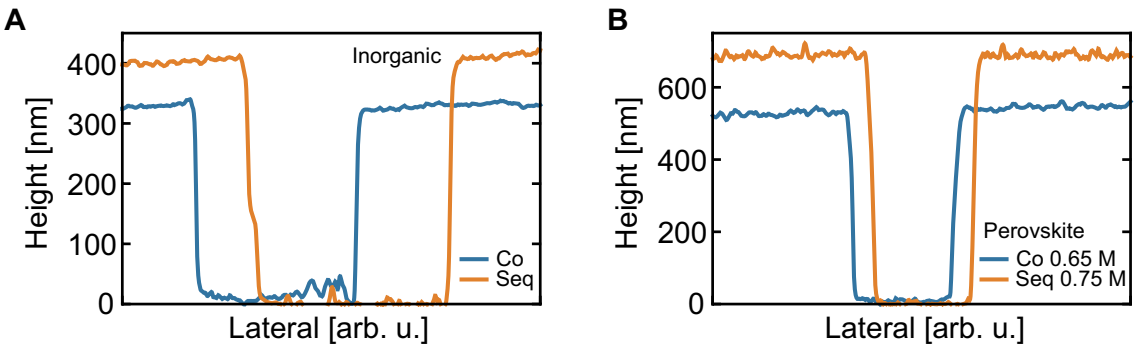

Figure S7: Surface profilometry of **A** the inorganic scaffold and **B** the perovskite film with optimal molarity of the organic cation solution for co-deposition (Co) and sequential deposition (Seq) of the inorganic scaffold. The expansion coefficients ($\text{thickness}_{\text{perovskite}}/\text{thickness}_{\text{inorganic}}$) of Co and Seq are 1.62 and 1.67, respectively, indicating a slightly increased organic cation uptake in case of sequentially deposited inorganic scaffolds.

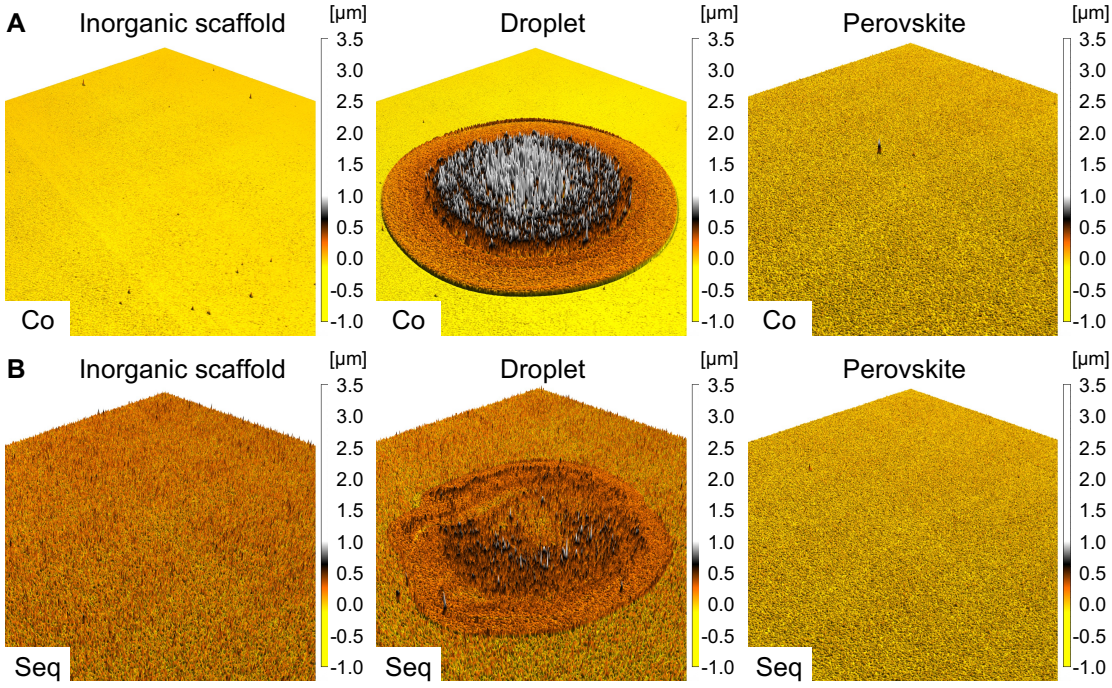

Figure S8: Surface structure analysis *via* confocal scanning microscopy for **A** co-deposition (Co) and **B** sequential deposition (Seq) of the inorganic scaffold. For better visibility, a 10-fold height magnification is chosen for all images. For the perovskite films, the optimal molarity of the organic cation solution is used.

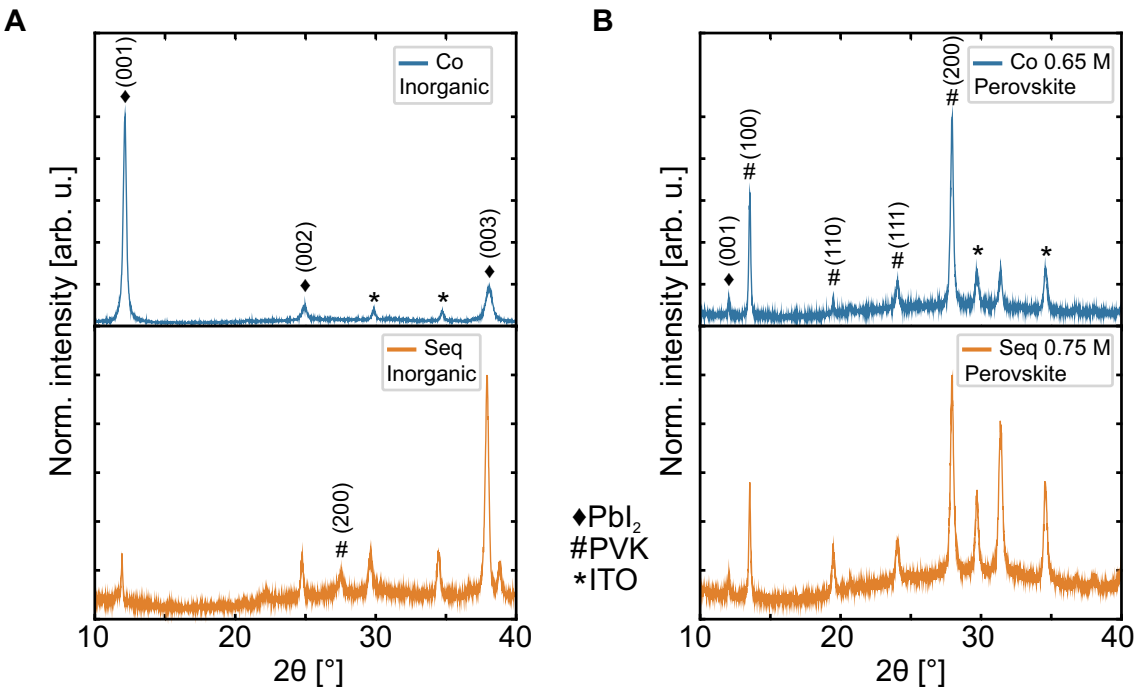

Figure S9: Normed X-ray diffraction (XRD) pattern for **A** the inorganic scaffold and **B** the perovskite film with optimal molarity of the organic cation solution for co-deposition (Co) and sequential deposition (Seq) of the inorganic scaffold. ♦ denotes the PbI_2 phase, # the perovskite phase and $*$ the indium tin oxide (ITO) phase.

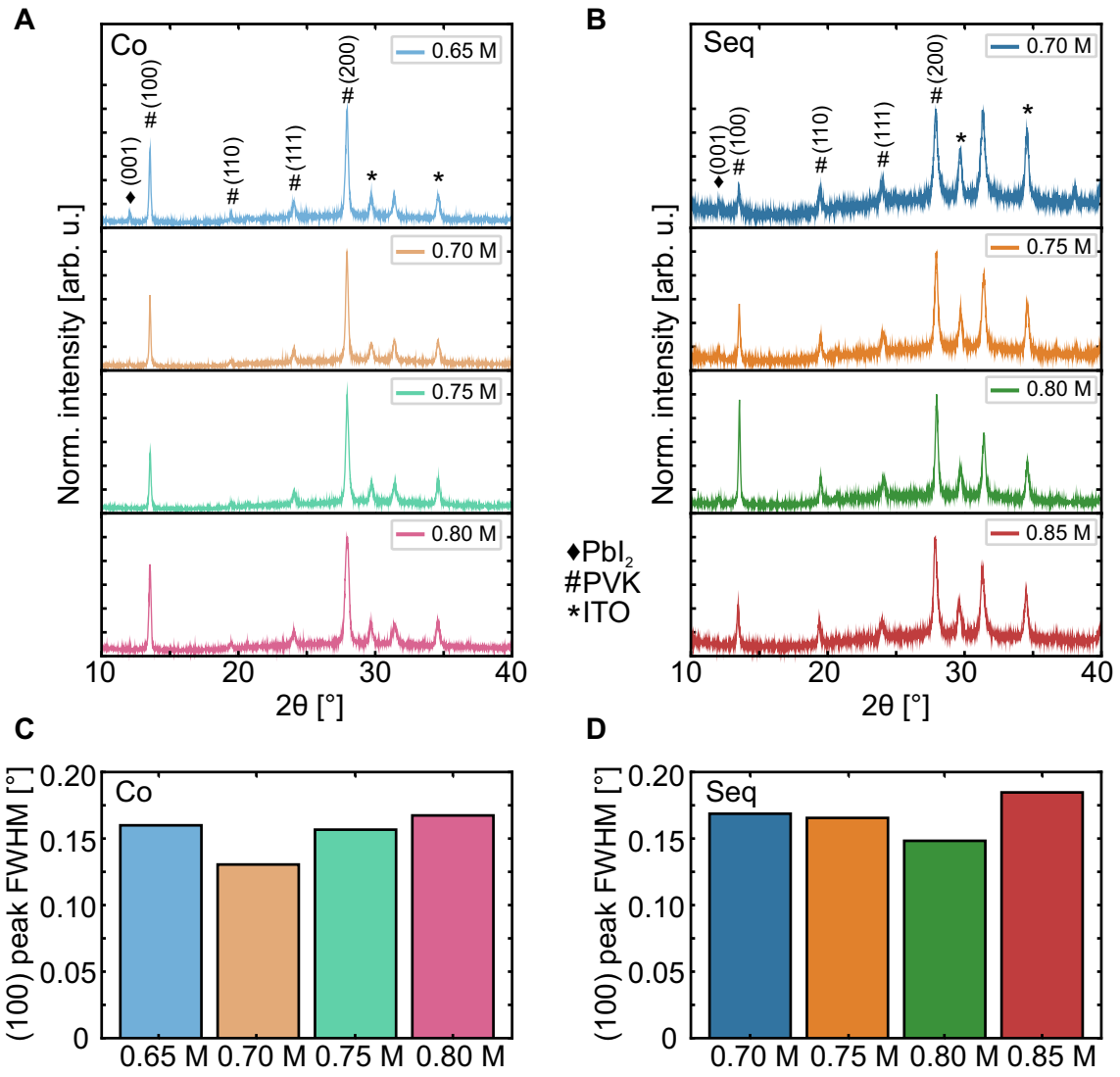

Figure S10: Normed X-ray diffraction (XRD) pattern for perovskite films with different molarities of the organic cation solution for **A** co-deposition (Co) and **B** sequential deposition (Seq) of the inorganic scaffold. ♦ denotes the PbI_2 phase, # the perovskite phase and $*$ the indium tin oxide (ITO) phase. Full width at half maximum (FWHM) of the (100) perovskite peak perovskite films with different molarities of the organic cation solution for **C** co-deposition (Co) and **D** sequential deposition (Seq) of the inorganic scaffold.

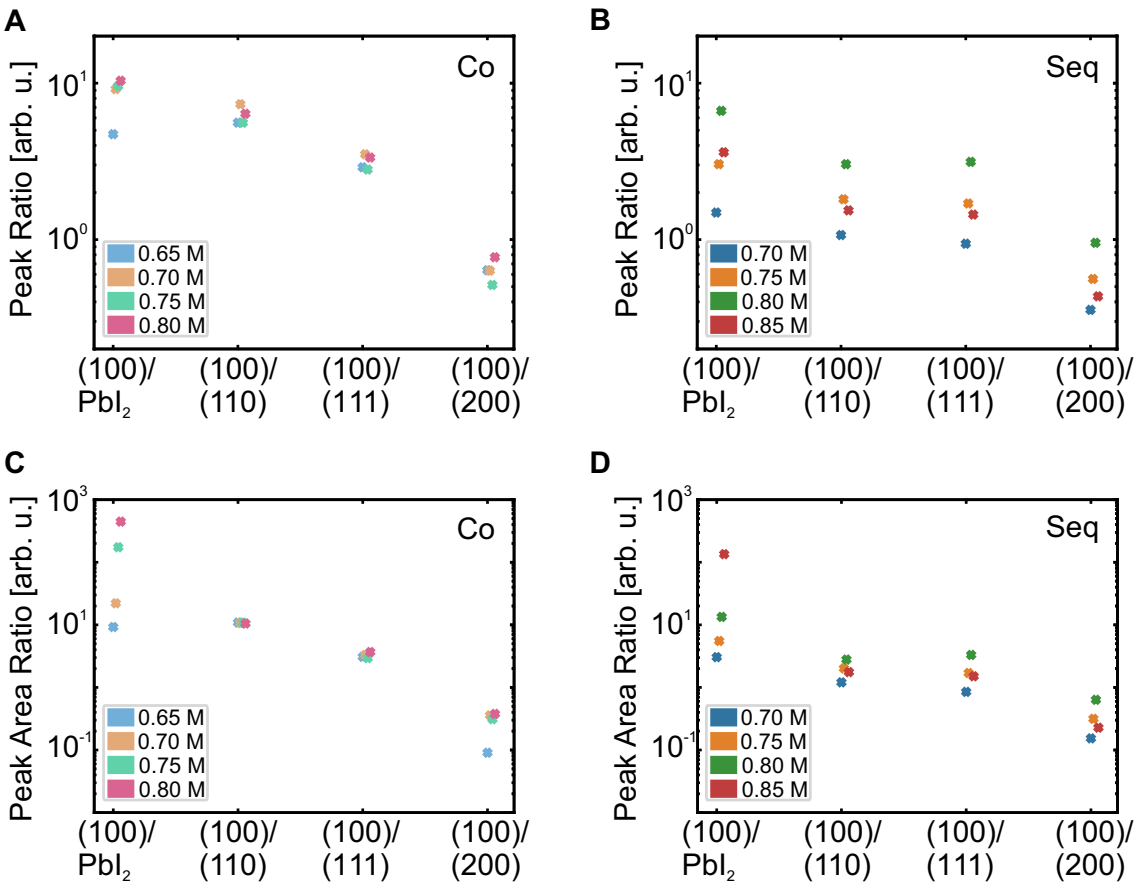

Figure S11: Peak intensity ratios as well as peak area ratios of the X-ray diffraction (XRD) pattern for perovskite films with different molarities of the organic cation solution for **A, C** co-deposition (Co) and **B, D** sequential deposition (Seq) of the inorganic scaffold.

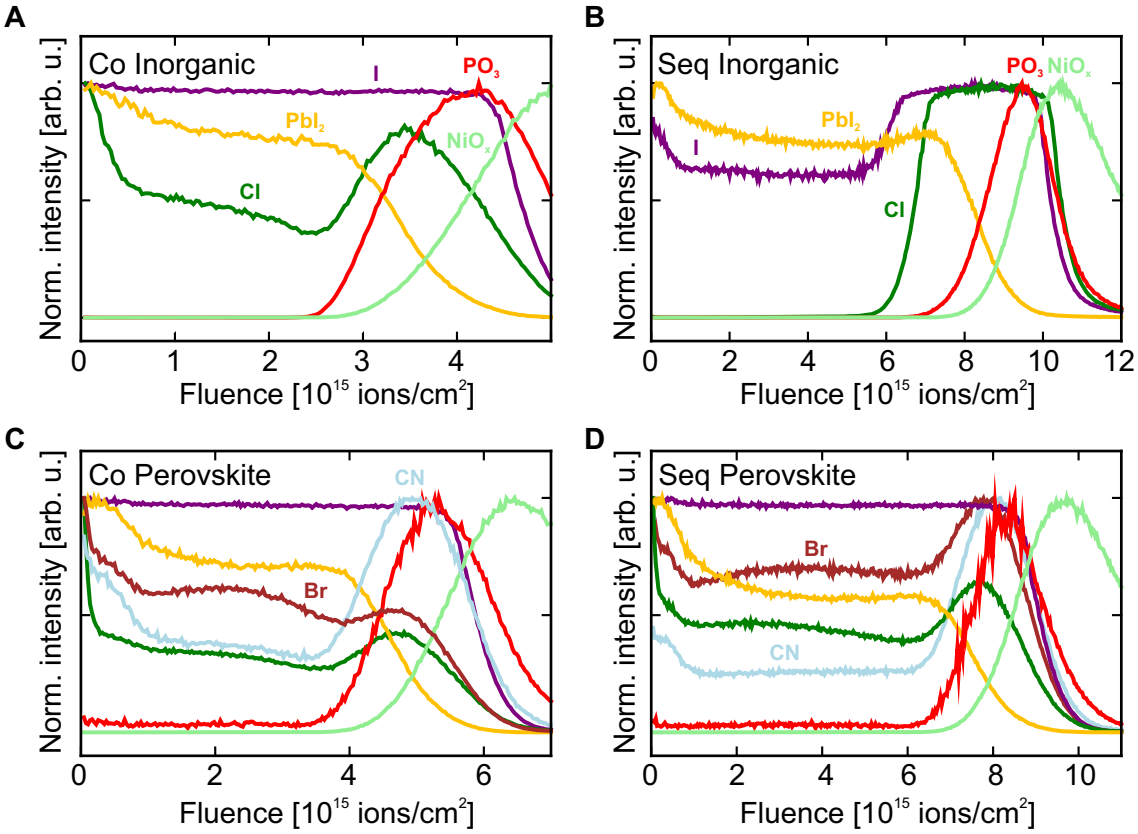

Figure S12: Normed time-of-flight secondary ion mass spectrometry (ToF-SIMS) measurements (negative polarity) of the inorganic scaffold deposited by **A** co-deposition (Co) and **B** sequential deposition (Seq), as well as of the final perovskite films with **C** co-deposition (Co) and **D** sequential deposition (Seq) of the inorganic scaffold. For the perovskite films, the optimal molarity of the organic cation solution is used. The following fragments are displayed: NiO_x: NiO_2^-; PO_3: $\Sigma(PO_3^-, PO_2^-)$; PbI_2: $^{207}PbI_3^-$; Cl: Cl^-; I: I^-; Br: Br^-; CN: CN^-.